COMPUTATIONAL ANALYSIS OF BASE FLOW/JET PLUME INTERACTION

E.M. Houtman[1], E. van der Weide[2], H. Deconinck[2], P.G. Bakker[1]

[1] Aerospace Engineering, Delft University of Technology, Kluyverweg 1, 2629 HS Delft, The Netherlands
[2] Aeronautics/Aerospace Dept, von Karman Institute, Waterloose Steenweg 72, B-1640 Sint Genesius-Rode, Belgium

ABSTRACT

Computations of the flow around a blunted cone-cylinder rocket model with a centrally protruding nozzle are presented. The computations are performed for supersonic free streams of Mach 2 and 3, while the jet exhausting from the nozzle had an exit Mach number of 4 and operated at various jet stagnation pressures, such as to have different jet exit pressure to ambient flow pressure ratios. These ratios all exceeded unity indicating that one had to do with under-expanded jetflow. The freestream Reynolds numbers based on the model length were greater than 5×10^6, thus the flow could be considered turbulent. The present investigation was part of a joint computational/experimental research program on base flows of rocket propelled vehicles.

Computational results of two codes based on the Reynolds Averaged Navier-Stokes equations are presented, a finite-volume code using 1D upwind schemes and structured multi-block grids, and a multi-dimensional upwind method on unstructured grids. Different turbulence models have been used. Computed results for several conditions are compared against each other and experimental data. The results show good agreement in those parts of the flow which are not dominated by viscous effects. The prediction of the base flow, however, is the most difficult problem.

Key words: base flow, turbulence modelling, multi-dimensional upwinding.

1 INTRODUCTION

For the development of the next generation reusable launchers one of the critical areas is concerned with the proper modelling of the base flow physics. In particular the base flow affects the aerodynamic characteristics (axial force) and the heat loading at the base of a vehicle may be considerable. To obtain more insight in this problem a combined experimental and computational study has been made within the framework of FESTIP (Future European Space Transportation Investigation Program) ‘Kuczera et al. 1996; Bannink et al. 1997; Bannink et al. 1998’. The experimental part of the investigation was concerned with the investigation of the flow field along an axisymmetric BETA II like configuration with a single operating exhaust nozzle. The model was positioned in a uniform supersonic free stream at zero angle of attack. The supersonic jet emanating from the centrally protruding exhaust nozzle in the base interacts with the external main flow around the model. In the interaction zone a turbulent mixing layer, a recirculation region and a shock system (plume shock, barrel shock) is formed.

This paper presents the results of numerical simulations of this flow. Two different computational methods are used. The first method is based on a multi-block finite-volume discretization using flux-(difference-)splitting schemes (van Leer, Osher, Roe). The computations are performed on a structured grid. Turbulent simulations are performed with the one-equation Spalart-Allmaras model. The second one uses a discretization technique based on a multi-dimensional upwind method on unstructured grids. Four turbulence models are considered: the two-equation models $k - \omega$, BSL (almost identical to $k - \varepsilon$ for this flow), SST, and the one-equation model of Spalart-Allmaras.

2 MODEL AND EXPERIMENTS

The selected geometry is axisymmetric having a spherically blunted cone as forebody and a cylinder of about the same length as the cone as afterbody. From the centre of the base a nozzle protrudes; its outside shape is a circular cylinder. The nozzle itself is conical with a total divergence of $15°$. This angle has been chosen to obtain a satisfactory radial flow at the nozzle exit and to minimize the possibility of flow separation. The exit diameter of the nozzle is about one third of the model base diameter. The conical forebody has a semi apex angle of $11°$ and a fair amount of bluntness in a nose radius of 7.5 mm. The cylindrical afterbody has a length of 90 mm and the total length of the model is 186.81 mm. Further details of the model are shown in Fig. 1. A more detailed description of the experiments is given by Bannink et al. (1997; 1998).

The boundary layer was tripped at 38 mm from the nose (40% of the cone length) by a copper wire with a thickness of 0.15mm. The measurements were performed at free stream Mach numbers of $M_\infty = 2$ and 3 and at stagnation pressures of $p_t = 2$ and 5.75 bar respectively; these values are nominal values. The stagnation temperature is in both cases the same and approximates room temperature: $T_t = 285\text{K} \pm 2\text{K}$. The jet stagnation pressure p_{t_j} was varied between 15 bar and 100 bar.

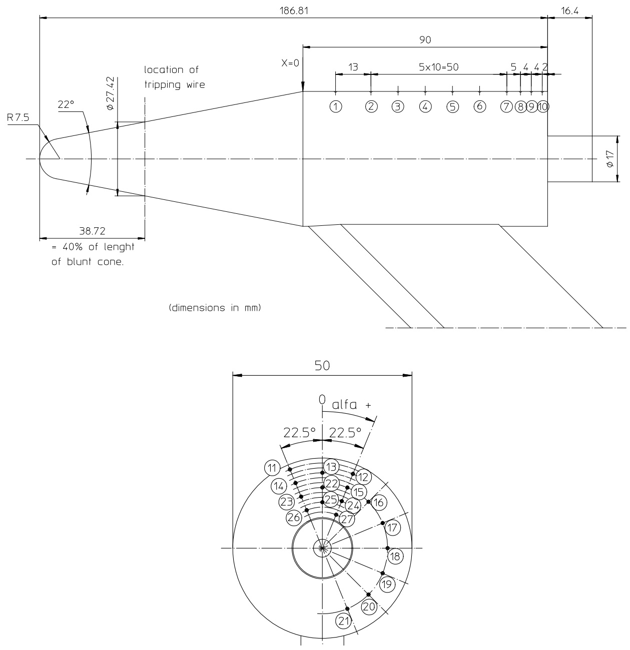

Fig. 1: *Location of pressure taps along body contour and at the base*

3 COMPUTATIONAL METHODS

3.1 Finite Volume Method

Numerical simulations were performed using a code based on a cell-centred finite-volume discretization of the Euler and Navier-Stokes equations 'Houtman et al. 1995'. This method is provided with second-order accurate upwind discretizations according to the flux-splitting scheme of van Leer and the flux-difference-splitting schemes of Osher and Roe. The results presented here are computed using the van Leer scheme. Higher order spatial discretizations are obtained with Monotonic Upstream Schemes for Conservation Laws (MUSCL), an interpolation technique with a van Albada limiter to suppress spurious oscillations at discontinuities. The viscous terms are discretized using central differences. The discretized equations are solved with an implicit line-Gauss-Seidel method within an efficient nonlinear multigrid solution procedure. Structured multiblock grids are used to compute flows around complex geometries.

The code is equipped with the one-equation Spalart-Allmaras turbulence model. The equations for the turbulent eddy viscosity are solved independent of the Navier-Stokes equations. An implicit backward Euler operator is used, which is solved using a Line-Gauss-Seidel iteration. The use of the Message Passing Interface (MPI) allows parallel processing on a cluster of workstations or a parallel computer (Cray T3E), in order to decrease CPU time.

3.2 Multi-dimensional Upwind Method

The multi-dimensional upwind method is well-established nowadays for scalar convection-diffusion problems for which it leads to improved schemes with compact stencils compared to the standard finite volume schemes based on MUSCL reconstruction 'Deconinck et al. 1993; Paillère and Deconinck 1995; Paillère et al. 1997'. The generalization to coupled systems has been made recently 'van der Weide and Deconinck 1996; van der Weide and Deconinck 1997' and is constructed such that for any decoupled equation in the system it automatically reduces to the scalar distribution scheme on which it is based. The discretization technique for the inviscid part is a monotonic second order, multi-dimensional upwind method, where the limiting is applied by means of a matrix limiter to the first order system N-scheme. The Petrov-Galerkin finite element interpretation of the schemes allows a straightforward discretization of the viscous terms. Through integration by parts, the discretization of these terms on linear elements boils down to the Galerkin method.

The time integrator is the backward Euler method, where the resulting linear system is solved by block preconditioned GMRES. For this purpose the AZTEC library of SANDIA is used, which allows a fully parallel implementation. First order Jacobians are used for the nonlinear scheme.

3.3 Turbulence models

The turbulence models used in this paper are either one-equation or two-equation models, which refers to number of additional transport equations added to the Navier-Stokes equations to model the turbulent flow field.

The following models are used:

- **Spalart-Allmaras:** This is an empirical one-equation model 'Spalart and Allmaras 1992', which solves some kind of a turbulent viscosity and is insensitive to the free-stream turbulence.
- **k$-\omega$ model:** This is a two-equation model 'Wilcox 1988' for the transport of the turbulent kinetic energy and its dissipation rate. Contrary to the $k-\epsilon$ model it does not require damping functions in the viscous sub-layer. The model is rather sensitive to disturbances in the free-stream turbulent quantities.
- **BSL model** The Baseline (BSL) two-equation model 'Menter 1994' is a modification of the $k-\omega$ model in order to decrease the sensitivity to disturbances in the turbulent quantities in the free-stream.

- **SST model** The two-equation Shear-Stress Transport (SST) model 'Menter 1994' uses the same transport equations for k and ω and the same blending function as the BSL model but the $k-\omega$ constants have been slightly changed. This improves the performance of the model in adverse pressure gradient flows.

4 COMPUTATIONS

4.1 Introduction

A selected number of experimental conditions has been calculated. With the structured grid finite volume method computations have been performed for two cases: $M_\infty = 1.96$, $p_{t_j}/p_\infty = 349.5$ and $M_\infty = 2.98$, $p_{t_j}/p_\infty = 193.5$. With the multi-dimensional upwind method only one case has been computed, $M_\infty = 2.98$ and $p_{t_j}/p_\infty = 193.5$.

The interior nozzle has been computed assuming a zero radial velocity at the subsonic inlet. In combination with the total conditions this completes the information needed to treat the subsonic inlet boundary. In the numerical simulations the shape of the nozzle upstream of the throat has been slightly changed, such that the inlet flow has a low subsonic Mach number. It is assumed that the influence of this approximation on the solution in the base region is negligible. In the experiments the exterior boundary layer has been tripped near the nose. With the structured finite-volume method transition has been specified at this position, while for the multi-dimensional upwind method a fully turbulent flow has been assumed in the computations.

4.2 Grid

For the structured finite-volume method, the computations are performed on multiblock grids consisting of 8 blocks, which were created using GridPro. Two grids were used: a coarse grid with a total of $29,824$ cells, and a fine grid with a total of $44,224$ cells. The fine grid is obtained from the coarse grid by a refinement in a direction normal to the surfaces with a factor of 2. A part of the coarse grid is given in Fig. 2 and a detailed view of the grid in the base region is given in Fig. 3.

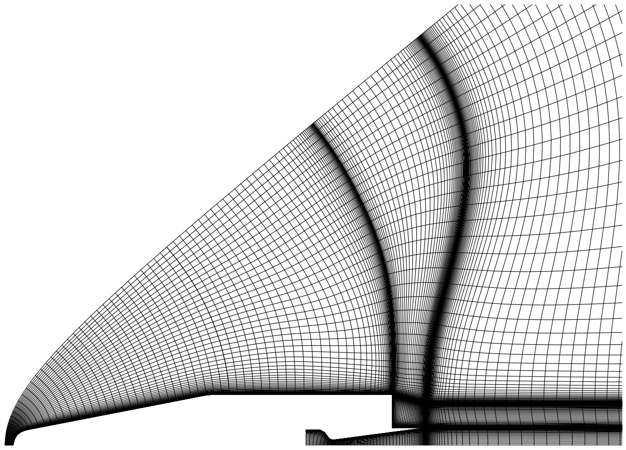

Fig. 2: *Structured grid*

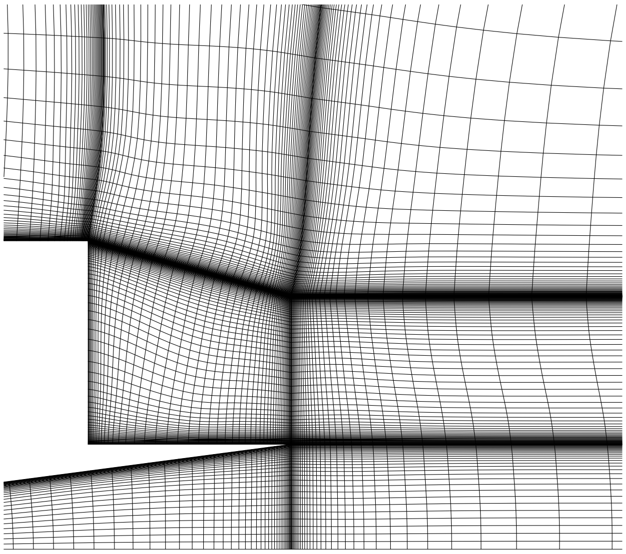

Fig. 3: *Detail of structured grid*

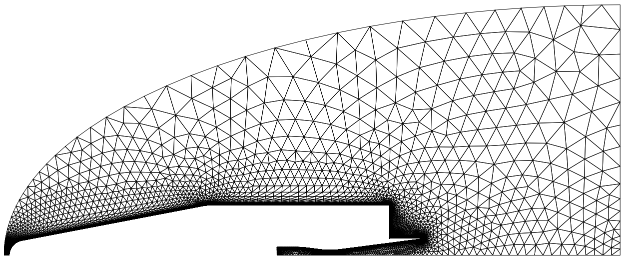

Fig. 4: *Unstructured coarse grid (15,505 nodes)*

The hybrid structured/unstructured approach 'Carette 1997' has been used to generate two grids for the multi-dimensional method. The coarse version, shown in figure 4, has 15,505 nodes, of which approximately 12,000 are located in the structured part near the walls. Due to the high Reynolds number the initial normal spacing is 10^{-6} m, leading to aspect ratios of more than 4000. As can be seen in figure 4, the unstructured part of the grid is quite coarse and in fact much too coarse to predict the flow field downstream of the exhaust nozzle accurately. Therefore a very fine grid consisting of 119,519 nodes has been created. The grid in the base region is shown in figure 5. To investigate the solution in this base region even in more detail, it has been computed separately on a 925×481 triangulated structured grid, which is on an average 5 times finer in

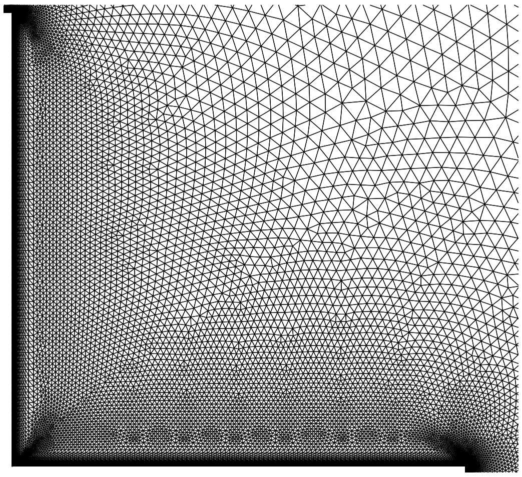

Fig. 5: *Base region of the unstructured fine grid (119,519 nodes)*

each coordinate direction than the grid shown in figure 5. The computational domain is a rectangular box, where the x-coordinate varies between 186.81 mm and 23.0 mm and the r-coordinate between 8.5 mm and 29.0 mm. On the inflow parts of the boundaries $x = 186.81$ mm, $y = 8.5$ mm and $y = 29.0$ mm a supersonic inlet has been assumed - the flow variables have been linearly interpolated from the second-order solution of the fine grid. The outflow boundary $x = 230$ mm has been chosen such that the flow is supersonic and consequently no boundary conditions need to be described there.

4.3 Results for the structured finite-volume method

4.3.1 $\mathbf{M_\infty = 1.96, p_{t_j}/p_\infty = 349.5}$

In order to obtain initial solutions for the turbulent flow computations, a series of Euler and laminar Navier-Stokes computations have been performed prior to the turbulent simulation. The convergence history of a typical case, including the Euler- and the laminar Navier-Stokes phase, computed on 8 processors of a Cray T3E, is given in Fig. 6. In the Euler- and the laminar Navier-Stokes phase the residual decreases 5 orders of magnitude; in the turbulent phase a decrease of about 2 orders of magnitude is obtained after about 3000 iterations. Monitoring the static pressure in a certain point at the base showed that a steady flow is obtained.

The Mach number isolines on the coarse grid for the cases $M_\infty = 1.96$, $p_{t_j}/p_\infty = 349.5$ and $M_\infty = 2.98$, $p_{t_j}/p_\infty = 193.5$ are given in Figs. 7 and 8, respectively. The different shocks (bow shock, plume shock and barrel shock), the slip line and the under-expanded jet can be observed. As the main characteristics of the flow are determined by inviscid phenomena, except in the base region, inviscid- and viscous solutions look very similar. This can be seen in Fig. 9, where the pressure dis-

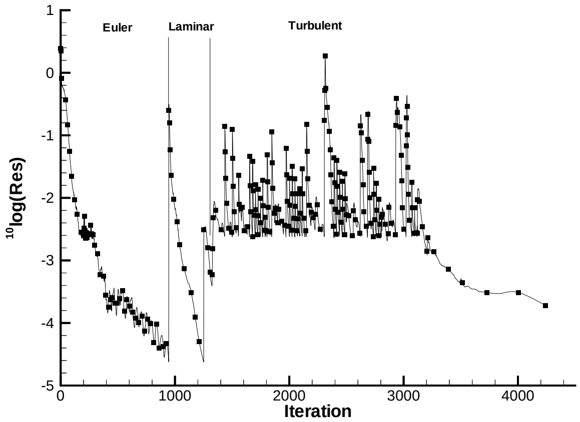

Fig. 6: *Residual and base pressure history for* $M_\infty = 2.98$, $p_{t_j}/p_\infty = 193.5$

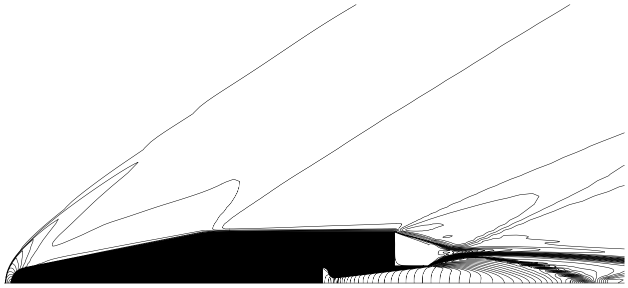

Fig. 7: *Mach isolines,* $M_\infty = 1.96$, $p_{t_j}/p_\infty = 349.5$, *turbulent computation,* $\Delta M = 0.15$

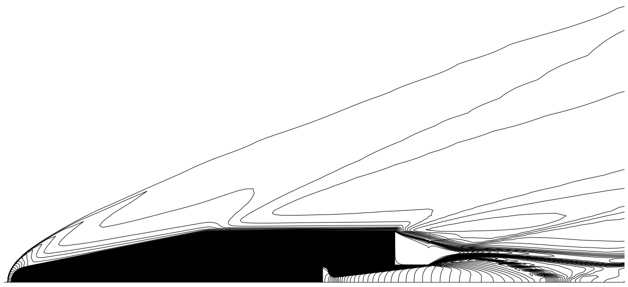

Fig. 8: *Mach isolines,* $M_\infty = 2.98$, $p_{t_j}/p_\infty = 193.5$, *turbulent computation,* $\Delta M = 0.15$

tribution on the cone-cylinder is given for the Euler- and the laminar and turbulent Navier-Stokes simulations, together with the experimental pressure distribution. Experiment and computations are nicely in accordance apart from two experimental data points; these are probably wrong due to irregularities of the pressure taps.

Some traverses with a pitot were performed in the base flow and in the jet flow at different free stream Mach numbers and jet stagnation pressures. In Fig. 10 the pitot pressures along the axis of the jet at $M_\infty = 1.96$ and $p_{t_j}/p_\infty = 349.5$ are compared with the computational results. The computational pitot pressures are obtained

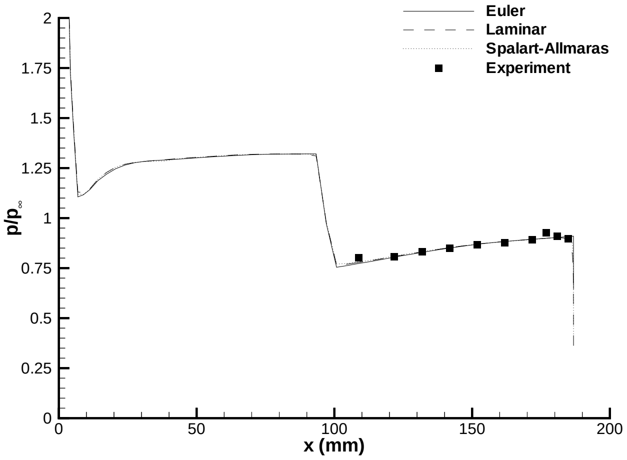

Fig. 9: *Cone-cylinder pressure distribution,* $M_\infty = 1.96$*,* $p_{t_j}/p_\infty = 349.5$*, computations and experiment*

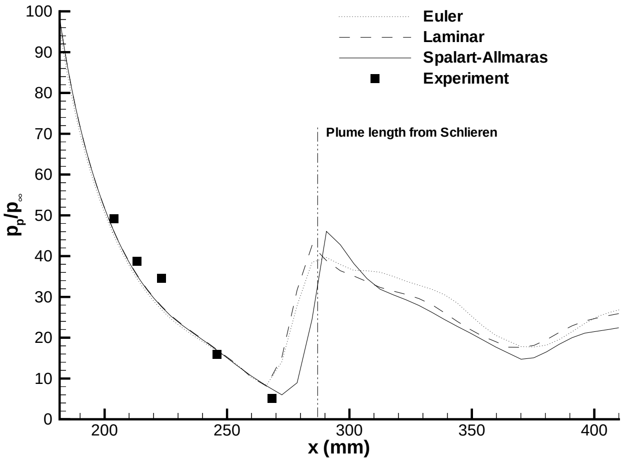

Fig. 10: *Computational and experimental pitot pressure distribution along jet core,* $M_\infty = 1.96$*,* $p_{t_j}/p_\infty = 349.5$*,* $r = 0$ *mm*

from the total pressure, which is corrected with the total pressure jump relation for an oblique shock. The agreement between experiment and computation is rather good. There is a significant difference between the computations with regard to the prediction of the position of the barrel shock at the jet axis. The barrel shock is visible due to the sudden increase in pitot pressure. In Fig. 10 also the position of the barrel shock as has been observed in the Schlieren visualization has been given.

In Figs. 11 to 13 some pitot pressure distributions along vertical lines in the base area and through the jet are plotted together with computed pitot pressures. The computed pitot pressures in the base region, $r < 25$ mm in Fig. 11, are lower than the measured pitot pressures. In this region a backflow occurs, which means that the pitot tube actually measures some static pressure. The computed pitot pressures, however, are not corrected for the flow direction.

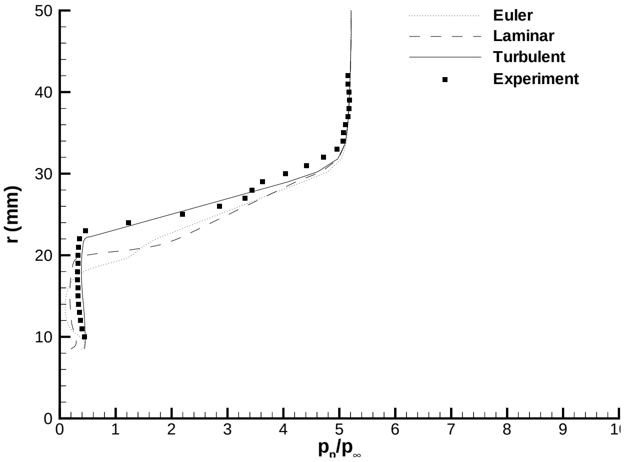

Fig. 11: *Computational and experimental pitot pressure distribution in base area,* $M_\infty = 1.96$*,* $p_{t_j}/p_\infty = 349.5$*,* $x = 197$ *mm*

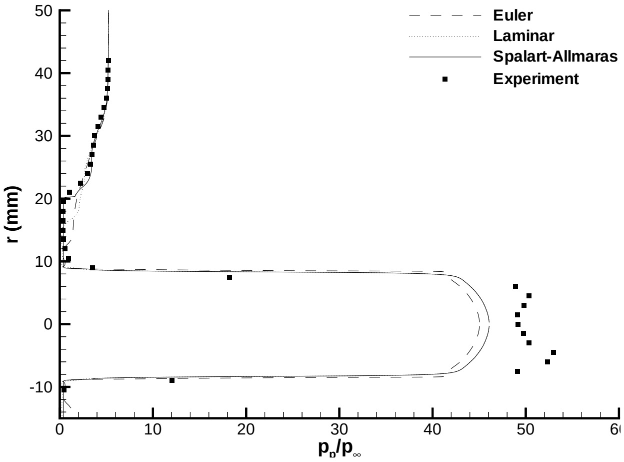

Fig. 12: *Computational and experimental pitot pressure distribution in base area,* $M_\infty = 1.96$*,* $p_{t_j}/p_\infty = 349.5$*,* $x = 204$ *mm*

The experimental and computational base pressure distribution for $M_\infty = 1.96$, $p_{t_j}/p_\infty = 349.5$ is given in Fig. 14 on the structured coarse grid. The Euler- and laminar simulations predict a base pressure which is much too low; the turbulent simulation with the Spalart-Allmaras model gives a base pressure which is only slightly lower than the experimental base pressures.

The experimental and computational base pressure distribution for $M_\infty = 2.98$, $p_{t_j}/p_\infty = 193.5$ is given in Fig. 15 on the structured coarse grid. The Euler- and laminar simulations predict a base pressure which is much too low, while the turbulent simulation with the Spalart-Allmaras model gives a base pressure which is slightly higher than the experimental base pressures. The base pressures of the viscous simulations on the coarse and the fine grid are compared in Fig. 16. The laminar solutions are almost identical, indicating grid convergence.

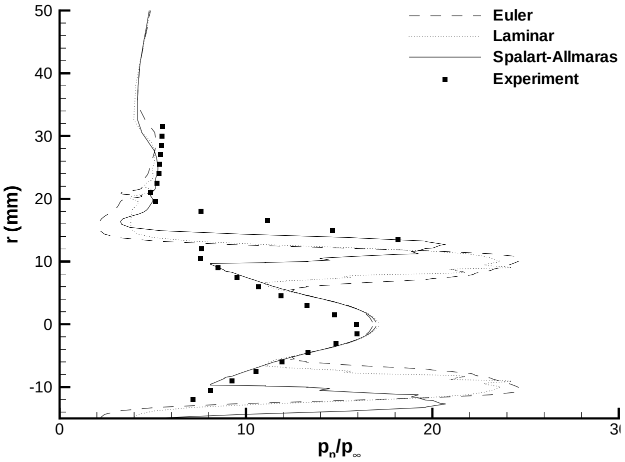

Fig. 13: *Computational and experimental pitot pressure distribution in base area,* $M_\infty = 1.96$, $p_{t_j}/p_\infty = 349.5$, $x = 246$ *mm*

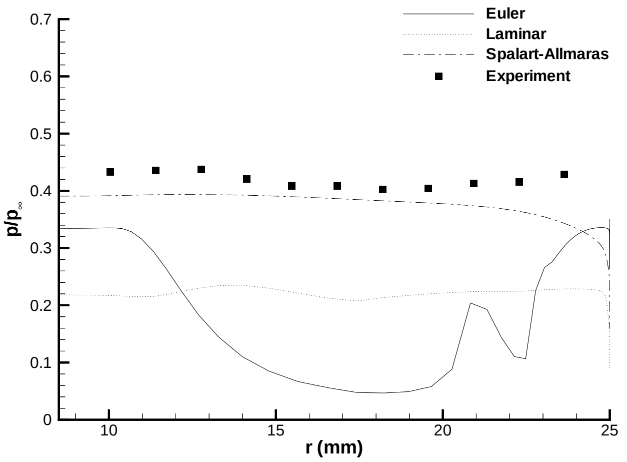

Fig. 14: *Base pressure distribution,* $M_\infty = 1.96$, $p_{t_j}/p_\infty = 349.5$, *Euler, laminar and turbulent computations compared with experiment*

The turbulent simulations are clearly not grid converged, and show a large disagreement with the experiment.

4.4 Results for the multi-dimensional upwind method

An initial solution on the fine grid has been obtained by interpolating the first-order coarse grid solution to this fine grid. The convergence history, starting from this solution, for the SST model, computed on 16 processors of the Cray T3E, is given in figure 17, which, shows a stalling of the second-order scheme. Due to stability reasons, the CFL number had to be restricted to 20, for both the first- and second-order computations in combination with numerical N-scheme Jacobians. At first glance this seems very low, but the explicit Runge-Kutta time integrators were unstable, regardless of the CFL number. These explicit schemes even failed for the first-

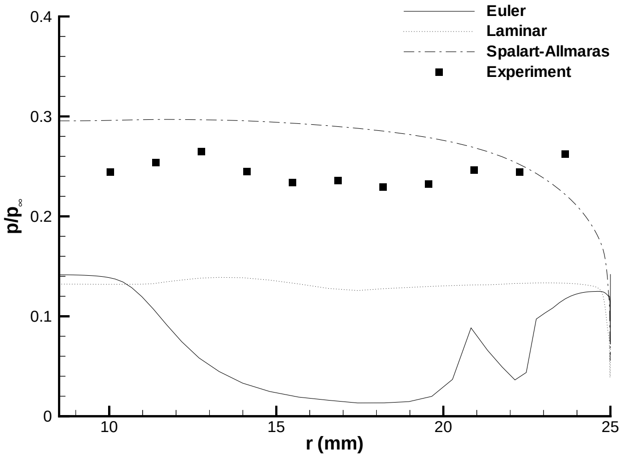

Fig. 15: *Base pressure distribution,* $M_\infty = 2.98$, $p_{t_j}/p_\infty = 193.5$, *coarse grid, Euler, laminar and turbulent computations compared with experiment*

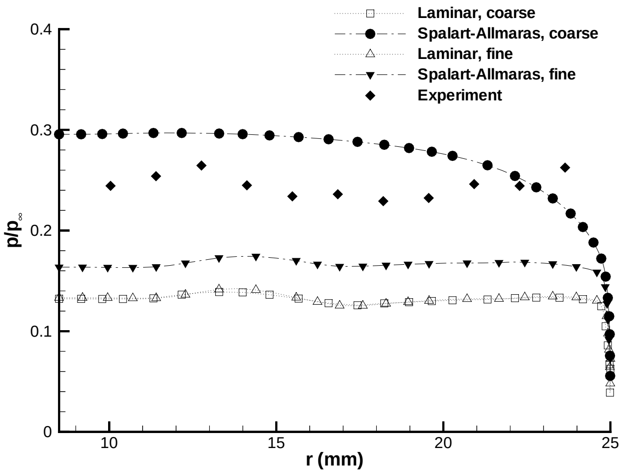

Fig. 16: *Base pressure distribution,* $M_\infty = 2.98$, $p_{t_j}/p_\infty = 193.5$, *coarse- and fine-grid laminar and turbulent computations compared with experiment*

order, laminar case, when restarting from the fully converged (implicit) solution. The total CPU-time for the two-equation models is approximately 19 hours; the solution in combination with the Spalart-Allmaras model could be obtained in 60% of this time.

Mach number isolines for the fine grid SST solution are depicted in figure 18. As the main characteristics of the flow are determined by inviscid phenomena, except in the base region, the solutions of the other turbulence models look very similar and are therefore not shown. The plume and barrel shock and the slip line in between are clearly visible, as well as the fact that the nozzle is underexpanded.

Computational and experimental pressure distributions

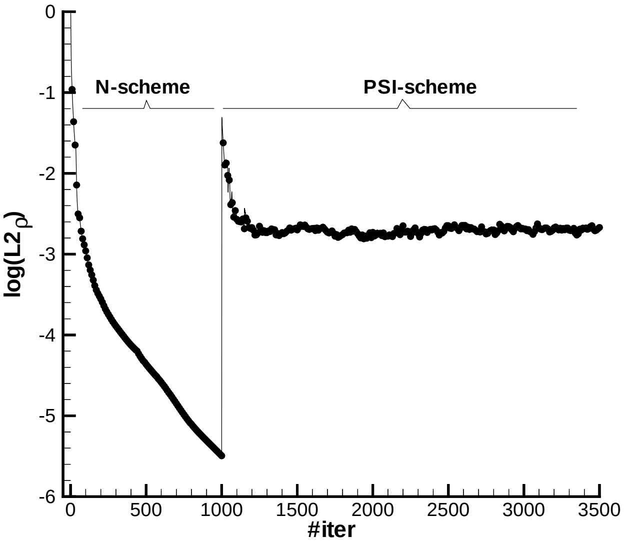

Fig. 17: *Convergence history for the rocket model on the fine grid, SST model.*

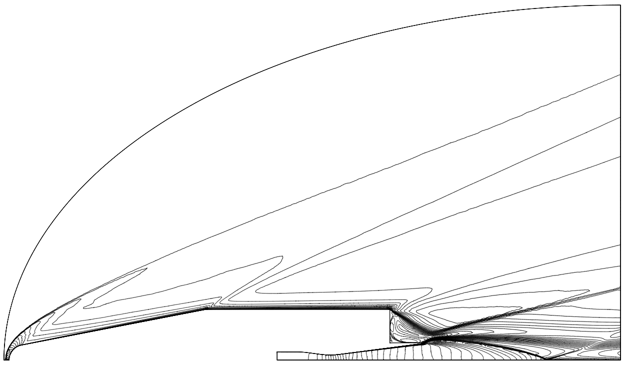

Fig. 18: *Mach number isolines for the rocket model, fine grid, SST turbulence model, PSI-scheme; step = 0.15.*

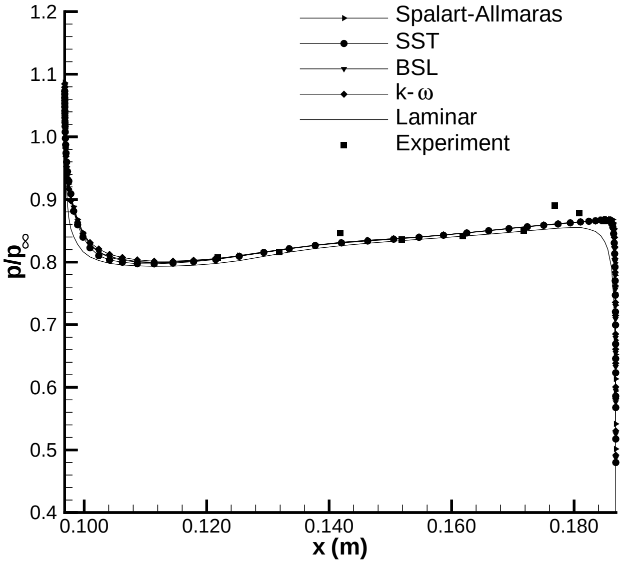

(a) coarse grid

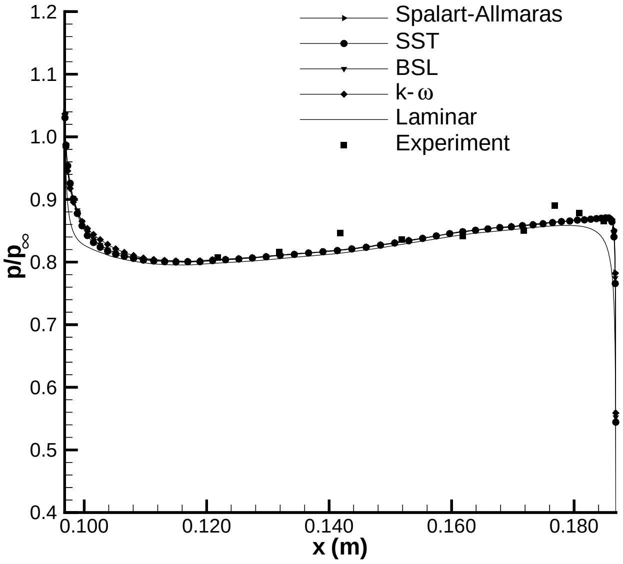

(b) fine grid

Fig. 19: *Computed and experimental pressure distribution on the cylindrical part for the rocket model*

for the coarse and fine grids on the cylindrical part of the model are shown in figure 19. It can be seen that the boundary layer thickness has some influence near the corners (compare the turbulent and laminar solutions), but the pressure in this part of the flow field is mainly determined by the inviscid equations. All results are nearly identical and fit the experimental data quite well. On the cylindrical part the solutions are grid converged, as both grids give the same results for all turbulence models.

An indication of the flow field can be seen in figure 20, which shows the computed streamlines based on the numerical solution of the SST model. Theoretically these streamlines must be closed because of mass conservation reasons, but due to integration errors this is numerically not possible. It is observed that four counter-rotating vortices are present in the base region. Consequently the flow is extremely complex and together with the fact that the Mach number is rather low in that area, this makes the problem very difficult to compute for a compressible flow solver.

Despite this, results have been obtained and the calculated pressure distributions in this region are compared with the experimental results in figure 21.

Especially from figure 21 (c) it is clear that the laminar solution is completely wrong. On the triangulated structured grid it is highly unsteady and consequently the pressure distribution shown only serves as illustration - it can be quite different some time steps later. Numerically Von Karman vortex sheets are observed. On the coarse and fine grid, see figure 21, the solution is steady, due to nu-

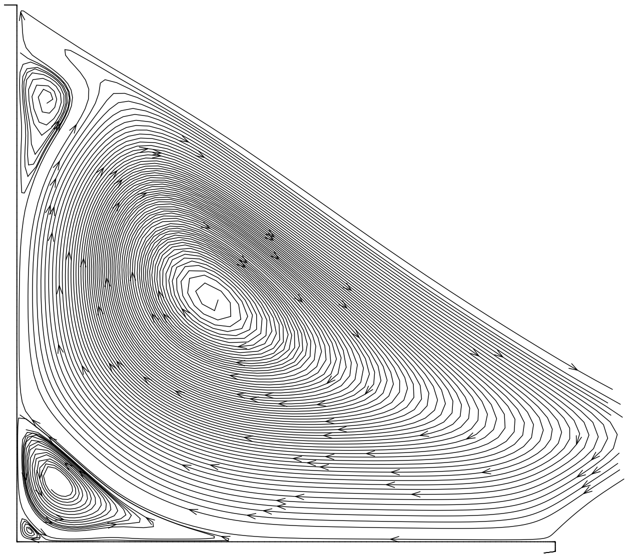

Fig. 20: *Computed streamlines in the base region of the rocket model for the SST turbulence model on the fine grid, PSI-scheme.*

merical diffusion. Note that the computed pressure distributions on these grids are a factor 3 too low compared with the experimental data.

All solutions on the coarse grid are not grid converged in the base region, as the computed pressures are lower than on the fine grid. The pressure distribution in the base region of the solution obtained with the Spalart-Allmaras model on the fine grid is identical to the distribution computed on the triangulated structured grid in the base region, see figures 21. Consequently this solution is grid converged. However, it is clear that the solutions of the two-equation models on the fine grid are not grid converged, as the base pressure distribution on the triangulated structured grid is 25 to 50% higher.

All turbulence models predict the base pressure too low compared to the experimental values. Taking into account the conclusion mentioned above, this difference is caused by the deficiency of the turbulence model in case of the Spalart-Allmaras model. For the two-equation models the situation is not so evident. As the base pressure distributions on the grids used differ quite a lot, the solutions cannot be assumed grid converged and it might be possible that on even finer grids the base pressure increases further. Furthermore, it is not clear what is the effect of imposing the entire solution (interpolated from the fine grid solution) on the inflow boundaries of the triangulated structured grid in the base region. There are indications that, especially in the interaction region between the exhaust plume and the base region, the solution changes quite a bit and thus a wrong solution is imposed there.

On the triangulated structured grid, figure 21 (c), the $k -$

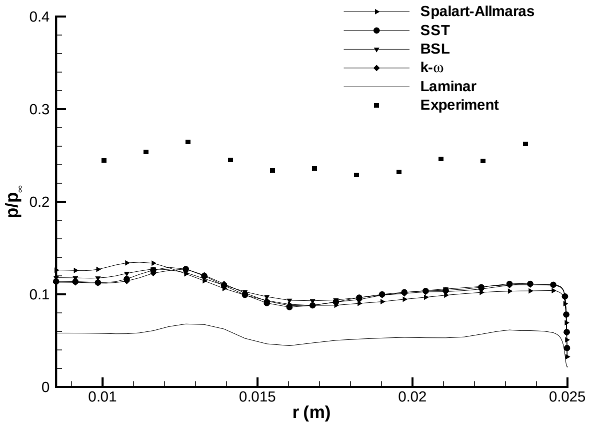

(a) coarse grid

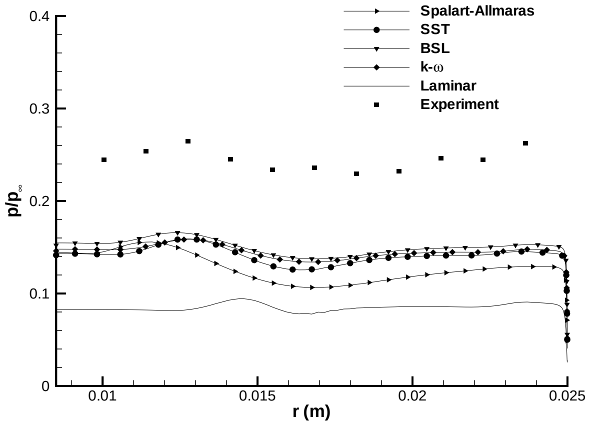

(b) fine grid

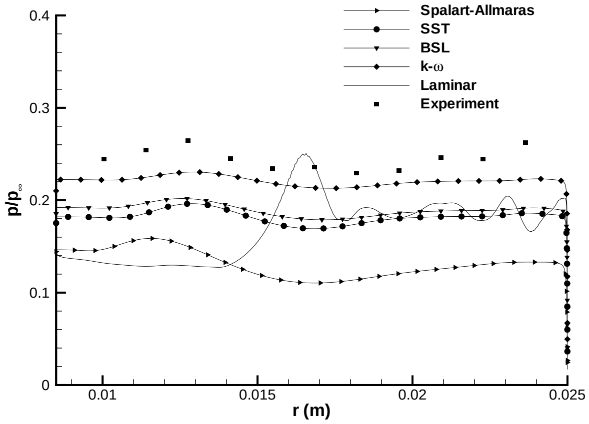

(c) veryfine grid

Fig. 21: *Computed and experimental base pressure distributions*

ω model predicts a significantly higher pressure in the base region than the BSL and SST-models, whose formulations are almost identical to the $k - \varepsilon$ model in this part of the flow field. Due to the limiting of the eddy-viscosity, the pressure distribution of the SST-model is slightly lower than the distribution obtained with the BSL-model. Furthermore, all two-equation models give a much higher pressure than the Spalart-Allmaras model on this grid.

5 CONCLUSIONS

Computational results of a single nozzle plume with a high supersonic exit Mach number of 4 exhausting in supersonic freestream flows of Mach 2 and 3 have been presented for a number of conditions. The Reynolds numbers at the base of the model were greater than 5×10^6 and in addition the boundary layer on the model was tripped.

The Euler and Navier-Stokes computations show a good agreement with the experiments in those regions which are not dominated by viscous effects. Most of the flow characteristics are modelled quite well.

The main conclusion is that the correct prediction of the base flow characteristics is a difficult problem, which requires extremely fine grids, especially for the two-equation models. The result obtained with the $k - \omega$ model on a very fine structured grid in the base region is surprisingly good, as it is believed that the base flow characteristic cannot be predicted accurately by eddy-viscosity turbulence models. Apparently this is not the case here, as long as sufficiently fine grids are used. However, it might be a coincidence and more cases should be computed to draw a decisive conclusion.

The computational effort to obtain a converged solution on the triangulated structured grid is enormous - ± 100 CPU hours on 16 processors of the Cray T3E for the two-equation models. The one-equation Spalart-Allmaras model does not need such fine grids, but the computed base pressure is almost a factor two too low.

It should be noted that only pressure distributions have been compared. An even more important, and probably also more difficult problem is the correct prediction of the heat flux in the base region, especially for hot plumes.

REFERENCES

Bannink, W.J., Bakker, P.G., and Houtman, E.M. 1997, *FESTIP AEROTHERMODYNAMICS: Experimental Investigation of Base Flow and Exhaust Plume Interaction*, Memorandum M-775, Dept. of Aerospace Engineering, Delft University of Technology

Bannink, W.J., Houtman, E.M., and Bakker, P.G. 1998, *Base Flow / Underexpanded Exhaust Plume Interaction in a Supersonic External Flow*, AIAA paper 98-1598-CP, AIAA 8th International Space Planes and Hypersonic Systems and Technologies Conference

Carette, J.-C. 1997, *Ph.D. thesis*, Université Libre de Bruxelles, Belgium

Deconinck, H., Struijs, R., Bourgois, G., and Roe, P. 1993, in *VKI LS 1993-04, Computational Fluid Dynamics*

Houtman, E.M., Bannink, W.J., and Timmerman, B.H. 1995, in *Proceedings of the Second European Symposium on Aerothermodynamics for Space Vehicles, ESTEC, Noordwijk, The Netherlands, November 21-25, 1994*, ESA SP-367, pp 517–522

Kuczera, H., Sacher, P., and Dujarric, C. 1996, *FESTIP System Study - An Overview*, IAF-96-V.3.02, 47th International Astronautical Congress, Beijing, China

Menter, F. 1994, *AIAA-Journal* **32(8)**, 1598

Paillère, H. and Deconinck, H. 1995, *Conf. on Num. Meth. for Euler and N-S equations, Montreal, Canada*

Paillère, H., Deconinck, H., and van der Weide, E. 1997, in *VKI LS 1997-02, Computational Fluid Dynamics*

Spalart, P. and Allmaras, S. 1992, *A One-Equation Turbulence Model for Aerodynamic Flows*, AIAA Paper 92-0439

van der Weide, E. and Deconinck, H. 1996, pp 747–753, Wiley, Proceedings of the 3rd European CFD Conference

van der Weide, E. and Deconinck, H. 1997, in *VKI LS 1997-02, Computational Fluid Dynamics*

Wilcox, D. 1988, *AIAA-Journal* **26(11)**, 1299